Journal of Materials Chemistry A

ROYAL SOCIETY OF CHEMISTRY

PAPER

View Article Online
View Journal | View Issue

Check for updates

Cite this: J. Mater. Chem. A, 2020, 8, 3246

A robust self-stabilized electrode based on Al-based metallic glasses for a highly efficient hydrogen evolution reaction†

Song Ju,‡[ab] Jingqing Feng,‡[abc] Peng Zou,[ab] Wei Xu,[ab] Shunjie Wang,[d] Weibo Gao,[d] Hua-Jun Qiu,[e] Juntao Huo*[ab] and Jun-Qiang Wang*[abf]

Received 29th October 2019
Accepted 8th January 2020

DOI: 10.1039/c9ta11867e

rsc.li/materials-a

An electrode with low performance or limited endurance for water splitting hydrogen generation has been the key limitation for application of hydrogen in contemporary clean-energy technologies. In this paper, an $Al_{80}Ni_6Co_3Mn_3Y_5Au_3$ metallic glass ribbon with outstanding catalytic activity in the hydrogen evolution reaction (HER) in acidic solutions is fabricated for the first time. Its overpotential is about 70 mV @ 10 mA cm^{-2} and Tafel slope is about 39 mV dec^{-1}, which are comparable to those of commercial noble Pt/C electrodes (33 mV @ 10 mA cm^{-2} and 38 mV dec^{-1}). Such a high catalytic reactivity is attributed to the synergic effect of multiple elements that disperse atomically homogeneously on the nanoporous surface. The outstanding catalytic activity persists and even becomes much better over a long-time reaction, which is attributed to the formation of a protective Au-rich layer in the interface. The Al-based metallic glass ribbon is flexible with high yield strength, large elasticity and good electrical conductivity, which are desirable and promising characteristics for a free-standing catalytic electrode in the HER.

Introduction

The hydrogen evolution reaction (HER) in aqueous solutions has been a promising strategy for promoting the application of hydrogen in clean energy applications. The exploration of high-performance, low-cost and durable catalysts is the most critical step to enhance the HER.[1–3] The most common electrocatalytic materials are powders, which need to be dispersed in a solvent and then fixed on a glassy carbon electrode by polymer binders (*e.g.* Nafion and PVDF).[1,4] However, a low loading amount and reduced electrical conductivity limit their applications.[5] Three-dimensional self-supporting electrode materials have been developed to solve these problems.[6–9] However, the mechanical strength of most self-supporting electrode materials is low,[10] which will severely limit their endurance.

Due to the limitations of traditional chemical synthesis methods, most of the synthesized materials are low-component alloys.[3,11–14] In recent decades, new processing technologies such as rapid solidification and mechanical alloying have become popular and can uniformly produce multi-component alloys such as amorphous materials.[15] Electrodes that are composed of multiple elements attract wide interest because the synergistic effect between different elements may exhibit superior catalytic activity.[16,17] For example, a CoFeP electrode exhibits significantly reduced hydrogen adsorption free energy compared to CoP.[17] Multi-component high entropy alloy nanoparticles exhibit almost 100% conversion in the ammonia oxidation reaction and nitrogen oxide selectivity.[16] Thus, exploring multicomponent catalysts is of special interest.

Metallic glasses are non-equilibrium materials, whose composition can be widely tuned beyond the maximum solubility of elements in equilibrium states.[18] Meanwhile, the performance of amorphous materials can be greatly improved by dealloying.[19] They are ideal model materials to fabricate catalyst electrodes with multiple components.[20–22] In this study, a multicomponent $Al_{80}Ni_6Co_3Mn_3Y_5Au_3$ (at%) metallic glass is developed and its catalytic activity in the HER is studied. Ni and Co are good catalytic elements and can form a nanoporous structure.[23] Y can increase glass forming ability.[24] Mn can increase the corrosion resistance of Al alloys.[25] Au has high

[a]Key Laboratory of Magnetic Materials and Devices, Zhejiang Province Key Laboratory of Magnetic Materials and Application Technology, Ningbo Institute of Materials Technology and Engineering, Chinese Academy of Sciences, Ningbo 315201, China. E-mail: juntaohuo@nimte.ac.cn; jqwang@nimte.ac.cn

[b]Center of Materials Science and Optoelectronics Engineering, University of Chinese Academy of Sciences, Beijing 100049, China

[c]School of Materials Science and Engineering, Shanghai University, Shanghai 200444, China

[d]Ningbo Institute of Measurement and Testing, Ningbo 315048, China

[e]School of Materials Science and Engineering, Harbin Institute of Technology, Shenzhen, 518055, China

[f]School of Materials Science and Engineering, Zhengzhou University, Zhengzhou 450001, Henan, China

† Electronic supplementary information (ESI) available. See DOI: 10.1039/c9ta11867e

‡ These authors contribute equally.

electrical conductivity and can form a nanoporous structure.[3] This metallic glass electrode is demonstrated to exhibit excellent electrocatalytic activity with a high catalytic current, low onset overpotential, and small Tafel slope in acidic electrolytes. The electrode also exhibits excellent tensile strength, electrical conductivity and performance stability as a self-supporting electrode.

Experimental

Materials fabrication and characterization

The master alloy with a nominal composition of $Al_{80}Ni_6Co_3Mn_3Y_5Au_3$ (at%) was fabricated by arc melting the high-purity elements (>99.9 wt%). The master alloy was re-melted in a quartz tube using induction melting and then injected onto a roller with a spinning tangent speed of about 40 m s^{-1} to get metallic glass ribbons. The thickness of the metallic glass electrode is 32 μm, the width of the electrode is about 1.8 mm, and the length is several meters. For electrochemical tests, a ribbon with a length of about 3–5 cm is cut from the long ribbon (Fig. S1†), and a length of 1 cm is exposed to the electrolyte with other parts protected by resin. To achieve better catalytic properties, a positive potential of 200 mV relative to an Ag/AgCl electrode is applied for 5000 s to dealloy the surface.

Electrochemical test

Electrochemical measurements were carried out at room temperature using an electrochemical workstation (Zahner Zennium) with a three-electrode system. The counter electrode is Pt foil; the reference electrode is Ag/AgCl (the concentration of Cl in the electrode is 3.5 M); the electrolyte was 0.5 M H_2SO_4 acid solution. Before HER experiments, a positive potential of 200 mV relative to the Ag/AgCl electrode is applied for 5000 s to activate the surface. The potential was converted to the reversible hydrogen electrode (RHE) according to eqn (1), $E_{(RHE)} = E_{(Ag/AgCl)} + 0.197 + 0.0592 \times pH$. A standard three-electrode method is applied to measure the electrical resistivity of metallic glass ribbons. Electrochemical impedance spectroscopy (EIS) is carried out with frequencies ranging from 100 000 Hz to 0.1 Hz with an amplitude of 10 mV at an overpotential of −70 mV.

Microstructure characterization

The microstructures of the metallic glass ribbons before and after the reaction are studied using a scanning electron microscope (SEM, Hitachi S4800), a transmission electron microscope (TEM Talos F200x), and an energy dispersive X-ray spectrometer (EDS Bruker 6I60). The TEM sample is prepared using a focused ion beam (FIB, Zeiss Auriga). The atomic packing structure of the ribbons is studied using X-ray diffraction (XRD, Bruker D8 Advance). The glassy nature is studied using differential scanning calorimetry (DSC, NETZSCH DSC-404-C).

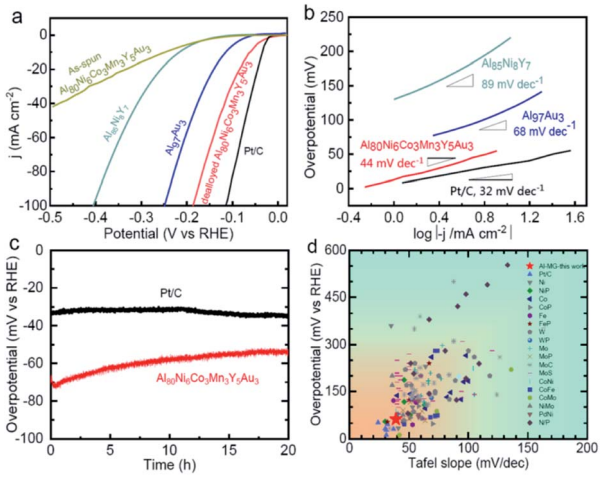

Fig. 1 Electrocatalytic property measurement. (a) Polarization curves measured at a scan rate of 5 mV s^{-1}. (b) Tafel plots for the $Al_{85}Ni_7Y_8$, $Al_{97}Au_3$, $Al_{80}Ni_6Co_3Mn_3Y_5Au_3$ and Pt/C electrodes derived from the HER polarization curves. (c) The $Al_{80}Ni_6Co_3Mn_3Y_5Au_3$ electrode is stable for more than 20 hours in 0.5 M H_2SO_4 at a hydrogen evolution current of 10 mA cm^{-2}. (d) Tafel slope *versus* overpotential at 10 mA cm^{-2} for more than 100 kinds of HER catalysts.

Results and discussion

Electrocatalytic properties

Fig. 1a shows the HER polarization curves. The dealloyed $Al_{80}Ni_6Co_3Mn_3Y_5Au_3$ electrode exhibits an exceptionally low overpotential (η) of about 62 mV at a current density (j) of 10 mA cm^{-2}. This is much smaller than that of the as-spun $Al_{80}Ni_6Co_3Mn_3Y_5Au_3$ metallic glass ribbon ($\eta = 251$ mV at $j = 10$ mA cm^{-2}), close to that of the commercial Pt/C electrode ($\eta = 33$ mV at $j = 10$ mA cm^{-2}) and much smaller than those of the $Al_{85}Ni_7Y_8$ electrode ($\eta = 230$ mV at $j = 10$ mA cm^{-2}) and the $Al_{97}Au_3$ electrode ($\eta = 142$ mV at $j = 10$ mA cm^{-2}), which verify the advantage of the multi-component synergic effect. Fig. 1b shows the Tafel plots for the three electrodes. The Tafel slope for the $Al_{80}Ni_6Co_3Mn_3Y_5Au_3$ electrode is about 44 mV dec^{-1}, which is close to that of the commercial Pt/C electrode (32 mV dec^{-1}) and much smaller than those of the $Al_{85}Ni_7Y_8$ metallic glass electrode (89 mV dec^{-1}) and the $Al_{97}Au_3$ crystalline electrode (74 mV dec^{-1}).

Considering the potential reaction between electrodes and the acid electrolyte, the stability of the material is a very important parameter. The constant-current stability at 10 mA cm^{-2} for the $Al_{80}Ni_6Co_3Mn_3Y_5Au_3$ metallic glass electrode is evaluated (Fig. 1c) with reference to the Pt/C electrode. It is amazing that the overpotential of the metallic glass electrode becomes smaller over time and reaches 51 mV after 20 hours. Fig. 1d compares the electrocatalytic performance in acidic electrolytes for more than 100 kinds of catalysts in dimensions of overpotential *versus* the Tafel slope. The $Al_{80}Ni_6Co_3Mn_3Y_5Au_3$ metallic glass electrode is among the most superior catalysts with both a small Tafel slope and small overpotential.

To verify the specific area of the electrode, its double-layer capacitance is evaluated by measuring the cyclic volt–ampere

curves at different sweep speeds (Fig. 2a). The capacitance of the double layer (C_{dl}) is about 9.6 mF cm^{-2}, which is much smaller than those of other HER electrodes.[1,26,27] This suggests that the intrinsic catalytic activity of this metallic glass ribbon should be excellent. To confirm this, the turnover frequency (TOF) is estimated to be about 0.5, 2.3, and 4.0 s^{-1} at 100, 150, and 200 mV, respectively (see Fig. 2b), which are among the highest values compared with those of other HER electrodes. Fig. 2c shows the Nyquist plot of the EIS results for $Al_{80}Ni_6Co_3Mn_3Y_5Au_3$, $Al_{97}Au_3$ and $Al_{85}Ni_8Y_7$ electrodes, which can be fitted using an equivalent circuit model (upper-right corner of the figure). In this model, R_s represents the resistance of the electrolyte and the R_{ct} represents the charge-transfer resistance that is related to the kinetics of the faradaic reaction of the HER. A smaller R_{ct} means a lower charge-transfer resistance and a better HER catalytic performance.[28–31] For the convenience of comparison, the fitting parameters (R_s and R_{ct}) of $Al_{80}Ni_6Co_3Mn_3Y_5Au_3$, $Al_{97}Au_3$ and $Al_{85}Ni_8Y_7$ electrodes are listed in Table 1. $Al_{80}Ni_6Co_3Mn_3Y_5Au_3$ exhibits the smallest value of $R_{ct} = 4.34$ ohm cm^2 among all the catalysts, implying the fastest charge-transfer process during the HER process.

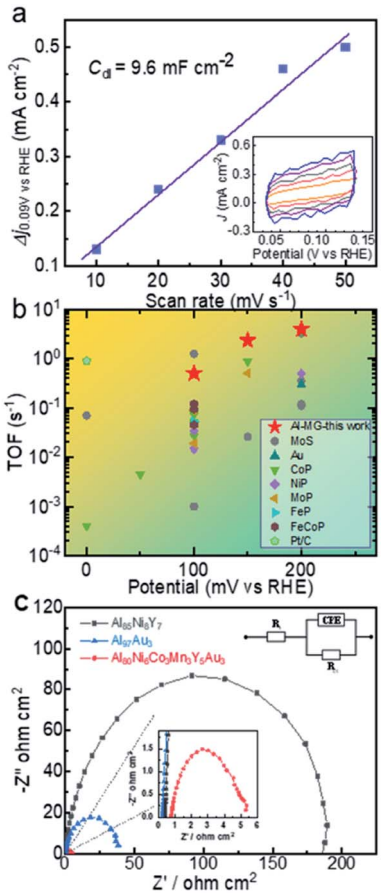

Fig. 2 (a) Current density (Δj) at 0.09 V *versus* scan rate to obtain C_{dl}. Inset shows the cyclic volt–ampere curves under different sweep speeds. (b) The turnover frequency (TOF) at different potentials for various electrodes. (c) EIS spectra of $Al_{85}Ni_7Y_8$, $Al_{97}Au_3$, and $Al_{80}Ni_6Co_3Mn_3Y_5Au_3$ obtained at an overpotential of 70 mV.

Table 1 Fitting parameters for EIS data of dealloyed $Al_{80}Ni_6Co_3Mn_3Y_5Au_3$, $Al_{97}Au_3$ and $Al_{85}Ni_8Y_7$ electrodes at a −70 mV overpotential

	$Al_{80}Ni_6Co_3Mn_3Y_5Au_3$	$Al_{97}Au_3$	$Al_{85}Ni_8Y_7$
R_s (ohm cm^2)	0.76	0.25	0.40
R_{ct} (ohm cm^2)	4.34	38.6	190.9

Microstructure characterization

The morphology of the metallic glass electrode is studied using SEM. The surface of the ribbon forms a uniform nanoporous layer of about 200 nm thick, and the inner side of the ribbon

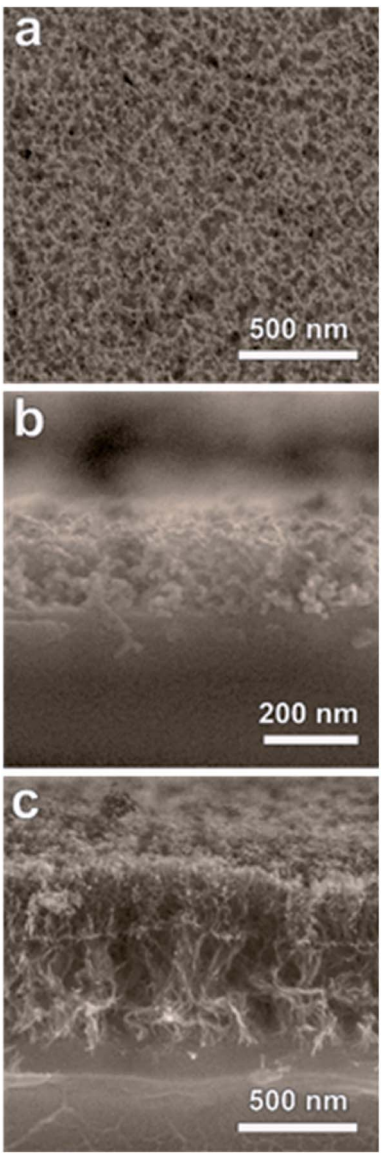

Fig. 3 (a) SEM images of the surface of the $Al_{80}Ni_6Co_3Mn_3Y_5Au_3$ ribbons after 2 h dealloying in 0.5 M H_2SO_4 at 200 mV (*versus* 3.5 M Ag/AgCl). (b) The corresponding cross sectional SEM image of the $Al_{80}Ni_6Co_3Mn_3Y_5Au_3$ ribbon dealloyed for 2 h, the thickness of the porous layer is about 200 nm. (c) The cross section of the ribbon reacted for 20 h at 10 mA cm^{-2}.

remains amorphous (Fig. 3a and b). After a 20 hour reaction, the thickness of the nanoporous layer increases to about 800 nm, which may be responsible for the enhancement of electrocatalytic performance. Given that the thickness of the metallic glass ribbon is about 32 μm, the nanoporous layer is about 1/40 of the total thickness of the metallic glass ribbon. This denotes that the metallic glass ribbon can survive up to 800 hours before completely turning into a 3D nanoporous structure.

The microstructure of the surface nanoporous layer is studied using high-resolution and scanning transmission electron microscopy (HRTEM & STEM), as shown in Fig. 4. The TEM image in Fig. 4a verifies that there are pits on the interface of metallic glass where the nanoporous ligaments grow. The selected area electron diffraction (SAED) patterns verify the amorphous structure of the metallic glass and the nanocrystalline structure of the nanoporous layer. The areal EDS scanning images confirm that most of the Al element has been dealloyed in the nanoporous layer. The nano-ligaments are composed of mainly Au with alloys of Ni, Co, Mn and Y, which are atomically homogeneously dispersed in Au. A thin AuNiCo rich layer is formed in the interface between the metallic glass and nanoporous layer, which benefits the corrosion resistance in acidic electrolytes and contributes to the high stability.

Mechanical properties and electrical conductivity

For free-standing electrodes, high fracture strength is desirable to guarantee the robust performance during cyclic loading in the charge–discharge reactions. High electrical conductivity is also desirable to allow the efficient charge transfer. Fig. 5a shows the tensile stress–strain curves of the $Al_{80}Ni_6Co_3Mn_3Y_5Au_3$ metallic glass electrode. The initial fracture strength of the metallic glass electrode is as high as 220 MPa. After a 2 hour reaction, the strength remains above 200 MPa. After 20 hours, it is still as high as 150 MPa. The electrical conductivity is measured to be about 2.6×10^6 S m^{-1}. Fig. 5b compares the strength and electrical conductivity for various electrodes. The $Al_{80}Ni_6Co_3Mn_3Y_5Au_3$ metallic glass electrode exhibits the highest strength and largest conductivity compared to other nanoporous intermetallics and bonded nanoparticle composites, which demonstrates its superiority as a free-standing electrocatalytic electrode.

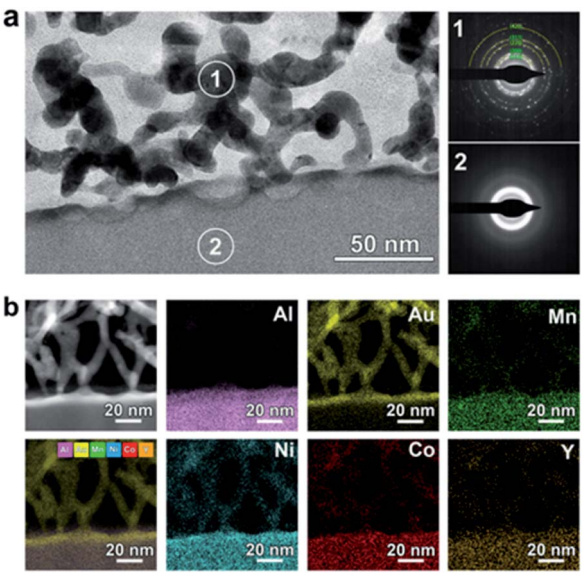

Fig. 4 (a) The TEM image of the amorphous matrix and the porous surface layer. The diameter of nanoligaments and the nanopores is about 10 nm. (1) The SAED diffraction rings of the porous layer confirm the nanocrystalline structure. (2) The SAED pattern of the matrix is a diffraction halo, which is a typical characteristic of amorphous phases. (b) The HAADF image and EDS map. It confirms that the Al element was dissolved during the reaction, and the Au element forms the ligaments with uniformly distributed Co, Ni, Mn, and Y elements.

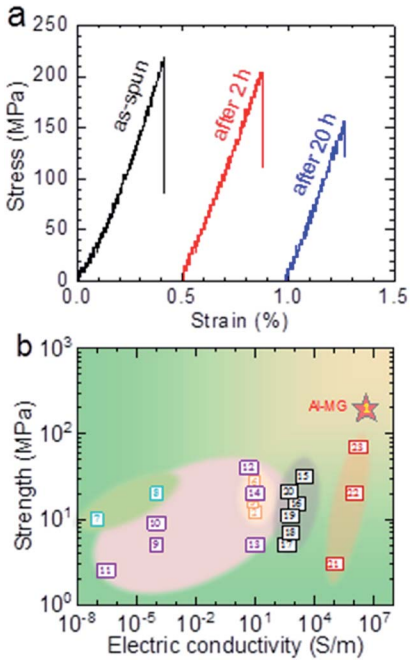

Fig. 5 (a) The tensile stress–strain curves of the metallic glass electrodes before and after the HER test (after 2 h and 20 h reactions). (b) The comparison of various HER electrodes in dimension of strength *versus* electrical conductivity. (1) Represents the Al-based metallic glass electrode, (2–6) hybrid electrodes with Nafion as the adhesive material, (7 and 8) hybrid electrodes with silica sol as the adhesive material, (9–14) hybrid electrodes with PVDF or PTFE as the adhesive material, (15–20) hybrid electrodes containing carbon nanotubes or carbon cloth, and (21–23) 3D nanoporous metals.

Discussion

The response kinetics of the catalysts is further evaluated by the corresponding Tafel plots. As shown in Fig. 1b, Tafel slopes are determined to be 32, 44, 74, and 89 mV dec^{-1} for commercial 20% Pt/C, $Al_{80}Ni_6Co_3Mn_3Y_5Au_3$, $Al_{97}Au_3$ and $Al_{85}Ni_8Y_7$ catalysts, respectively. A smaller Tafel slope illustrates that the HER rate increases more rapidly with increasing overpotential. There are three principal steps for the HER in acidic electrolytes, including the Volmer, the Heyrovsky, and the Tafel steps. First, a hydrated proton gains an electron and chemically attaches on the catalyst (*), namely, a Volmer reaction. After that, the adsorbed H (H*) tends to form H_2 *via* the Heyrovsky or Tafel

route, and sequentially desorbs. As for the Heyrovsky route, the generated H* combines with a hydrated proton, and then receives an electron from the catalyst surface to form H_2. In contrast, the Tafel route produces H_2 *via* the direct combination of two H* atoms. The Tafel, Heyrovsky, and Volmer reactions have Tafel slopes of 30, 40, and 120 mV per decade, respectively. Thus, the measured Tafel slope of 44 mV dec^{-1} for the $Al_{80}Ni_6Co_3Mn_3Y_5Au_3$ indicates a Volmer–Heyrovsky mechanism.

The exchange current density (J_0) represents the current density when the potential is zero in the Tafel plot. It is a key parameter that represents the catalytic efficiency. J_0 of the $Al_{80}Ni_6Co_3Mn_3Y_5Au_3$ catalyst is determined to be about 5.2×10^{-4} A cm^{-2}, which is close to that of the Pt/C electrode (6.9×10^{-4} A cm^{-2}) and much higher than those of $Al_{97}Au_3$ (1.4×10^{-4} A cm^{-2}) and $Al_{85}Ni_8Y_7$ (0.37×10^{-4} A cm^{-2}). This confirms the remarkable electron migration ability in the dealloyed $Al_{80}Ni_6Co_3Mn_3Y_5Au_3$ metallic glass electrode.

The TOF value of the $Al_{80}Ni_6Co_3Mn_3Y_5Au_3$ metallic glass electrode is 0.5 s^{-1} at an overpotential of 100 mV, which is much higher than those of most catalysts (Fig. 2b). The TOF values of the materials are calculated based on the amount of all atoms rather than the amount of active sites. So the TOF values might be underestimated in this paper. In conclusion, the main reason for the excellent catalytic performance of the materials is the increase in intrinsic catalytic activity.

Nanoporous Au has been applied as a supporting material for the deposition of catalysts because of its high conductivity. The HER activity of nanoporous Au is still limited because of its positive adhesion energy with atomic H.[32] The high HER efficiency observed in this work is mainly attributed to the large amount of atomic doping of Ni, Co, and Mn in Au ligaments. The combination of various elements probably exhibits a synergic effect during the catalytic reaction and enhances the HER activity. On the other hand, the low adhesion energy of hydrogen on Al and Au[32,33] benefits the release of the reduction product and accelerates the hydrogen evolution reaction.

The nanoligaments in the porous surface are very stable (HRTEM) without any thickening during a long-term test. Such a stable characteristic should be attributed to the sluggish diffusion in the multiple component alloys, which has been widely observed in high-entropy alloys.[34,35] For comparison, a simple alloy $Al_{97}Au_3$ (see ESI†) is studied for long term endurance. The Au nano-ligaments coarsen and the nanopores close after the 2 h reaction, which cause the sharp drop of reaction activity. Thus, the multiple component design strategy not only benefits the HER activity but also enhances the stability. At the same time, it was observed that the performance of the catalyst was continuously optimized with time. It is speculated that this is because the Al element in the amorphous matrix gets dissolved into the solution during the constant current process, which exposes more active sites to improve catalytic activity. This phenomenon was also confirmed by SEM testing (Fig. 3).

Conclusions

In summary, the $Al_{80}Ni_6Co_3Mn_3Y_5Au_3$ metallic glass ribbons are fabricated using a scalable melt-spinning technique. This metallic glass electrode contains little noble element but exhibits comparable catalytic reactivity with regard to the commercial noble Pt/C electrode. The electrode exhibits high strength that is desirable for a self-supporting electrode. Its high electrical conductivity and long-term endurance in reactions is preferred for catalytic reactions. The combined advanced properties bestow Al-based metallic glass as a promising candidate free-standing electrode for catalytic reactions.

Conflicts of interest

There are no conflicts to declare.

Acknowledgements

S. J. and J. Q. F. contributed equally to this work. The financial support from National Key R&D Program of China (2018YFA0703604 and 2018YFA0703602), National Natural Science Foundation of China (NSFC 51922102, 51811530101, 51771216, 51701230, and 51827801), Ningbo Science and Technology Inovation 2025 Project (2019B10051), Shenzhen Fundamental Research Program (JCYJ20180306171644942) and Zhejiang Provincial Natural Science Foundation of China (LR18E010002) is acknowledged.

Notes and references

1 J. Wang, F. Xu, H. Y. Jin, Y. Q. Chen and Y. Wang, *Adv. Mater.*, 2017, **29**, 1605838.
2 D. C. Giovanni, W. A. Wang, S. Nowak, J. M. Grenèche, H. Lecoq, L. Mouton and M. Giraud, *ACS Catal.*, 2014, **4**, 681–687.
3 Y. Ding and M. W. Chen, *MRS Bull.*, 2009, **34**, 569–576.
4 Q. Z. Xiong, Y. Wang, P. F. Liu, L. R. Zheng, G. Z. Wang, H. G. Yang and P. K. Wong, *Adv. Mater.*, 2018, **30**, 1801450.
5 Y. P. Zhu, Y. P. Liu, T. Z. Ren and Z. Y. Yuan, *Adv. Funct. Mater.*, 2015, **25**, 7337–7347.
6 Z. Lv, N. Mahmood, M. Tahir, L. Pan, X. W. Zhang and J. J. Zou, *Nanoscale*, 2016, **8**, 18250–18269.
7 N. K. Chaudhari, H. Jin, B. Kim and K. Lee, *Nanoscale*, 2017, **9**, 12231–12247.
8 Y. W. Tan, H. Wang, P. Liu, C. Cheng, F. Zhu, A. Hirata and M. W. Chen, *Adv. Mater.*, 2016, **28**, 2951–2955.
9 H. J. Qiu, Y. Ito, W. Cong, Y. Tan, P. Liu, A. Hirata and T. Fujita, *Angew. Chem., Int. Ed.*, 2015, **54**, 14031–14035.
10 H.-J. Jin, J. Weissmüller and D. Farkas, *MRS Bull.*, 2018, **43**, 35–42.
11 Q. W. Zhou, Z. H. Shen, C. Zhu, J. C. Li, Z. Y. Ding, P. Wang and F. Pan, *Adv. Mater.*, 2018, **30**, 1800140.
12 H. J. Zhang, X. P. Li, A. Hahnel, V. Naumann, C. Lin, S. Azimi and S. L. Schweizer, *Adv. Funct. Mater.*, 2018, **28**, 1706847.
13 Q. P. Yang, C. C. Lv, Z. P. Huang and C. Zhang, *Int. J. Hydrogen Energy*, 2018, **43**, 7872–7880.
14 J. S. Sun, Z. Wen, L. P. Han, Z. W. Chen, X. Y. Lang and Q. Jiang, *Adv. Funct. Mater.*, 2018, **28**, 1706127.
15 J. W. Yeh, S. K. Chen, S. J. Lin, J. Y. Gan, T. S. Chin, T. T. Shun and C. H. Tsau, *Adv. Eng. Mater.*, 2004, **6**, 299–303.

16 Y. G. Yao, Z. N. Huang, P. F. Xie, S. D. Lacey, R. J. Jacob, H. Xie and F. J. Chen, *Science*, 2018, **359**, 1489–1494.
17 Y. W. Tan, H. Wang, P. Liu, Y. H. Shen, C. Cheng, A. Hirata and T. Fujita, *Energy Environ. Sci.*, 2016, **9**, 2257–2261.
18 W. H. Wang, *Prog. Mater. Sci.*, 2007, **52**, 540–596.
19 C. W. Sun, Y. C. Hu and C. X. Sun, *ChemCatChem*, 2019, **11**, 2401.
20 J.-Q. Wang, Y.-H. Liu, M.-W. Chen, G.-Q. Xie, D. V. Louzguine-Luzgin, A. Inoue and J. H. Perepezko, *Adv. Funct. Mater.*, 2012, **22**, 2567–2570.
21 Y. C. Hu, Y. Z. Wang, R. Su, C. R. Cao, F. Li, C. W. Sun and Y. Yang, *Adv. Mater.*, 2016, **28**, 10293–10297.
22 S. X. Liang, Y. J. Liu, W. C. Zhang, W. M. Wang and L. C. Zhang, *Applied Materials Today*, 2020, **19**, 100543.
23 D. Strmcnik, P. P. Lopes, B. Genorio, V. R. Stamenkovic and N. M. Markovic, *Nano Energy*, 2016, **29**, 29–36.
24 P. P. Wang, J. Q. Wang, H. Li, H. Yang, J. T. Huo, J. G. Wang and C. T. Chang, *J. Alloys Compd.*, 2017, **701**, 759–767.
25 M. Zamin, *Corrosion*, 1981, **37**(11), 627–632.
26 L. Zuo, R. Li, Y. Jin and T. J. Zhang, *J. Electrochem. Soc.*, 2018, **165**, F207–F214.
27 W. C. Xu, S. L. Zhu, Y. Q. Liang, Z. D. Cui, X. J. Yang and A. J. Inoue, *J. Mater. Chem. A*, 2018, **6**, 5574–5579.
28 L. C. Zhang, Z. Jia, F. Lyu, S. X. Liang and J. Lu, *Prog. Mater. Sci.*, 2019, **105**, 100576.
29 S. X. Liang, Z. Jia, Y. J. Liu, W. C. Zhang, W. M. Wang, J. Lu and L. C. Zhang, *Adv. Mater.*, 2018, **30**, 1802764.
30 Z. Jia, X. G. Duan, P. Qin, W. C. Zhang, W. M. Wang, C. Yang, H. Q. Sun, S. B. Wang and L. C. Zhang, *Adv. Funct. Mater.*, 2017, **27**, 1702258.
31 Z. Jia, Q. Wang, L. Sun, Q. Wang, L. C. Zhang, G. Wu, J. H. Luan, Z. B. Jiao, A. D. Wang, S. Z. Liang, M. Gu and J. Lu, *Adv. Funct. Mater.*, 2019, **29**, 1807857.
32 B. Hinnemann, P. G. Moses, J. Bonde, K. P. Jørgensen, J. H. Nielsen, S. Horch and I. Chorkendorff, *J. Am. Chem. Soc.*, 2005, **127**, 5308–5309.
33 M. Curioni and F. Scenini, *Electrochim. Acta*, 2015, **180**, 712–721.
34 Y. Zou, H. Ma and R. Spolenak, *Nat. Commun.*, 2015, **6**, 7748.
35 Y. Zhang, T. T. Zuo, Z. Tang, M. C. Gao, K. A. Dahmen, P. K. Liaw and Z. P. Lu, *Prog. Mater. Sci.*, 2014, **61**, 1–93.